COBEM 2023 27TH INTERNATIONAL CONGRESS OF MECHANICAL ENGENEERING

ABCM Brazilian Society of Mechanical Sciences and Engineering
27th ABCM International Congress of Mechanical Engineering
December 04-08, 2023, Florianópolis-SC, Brazil

COB-2023-1068
ON THE DYNAMIC BEHAVIOR OF A ONE-DIMENSIONAL METAMATERIAL POSSESSING INERTIAL AMPLIFICATION MECHANISM COMBINED WITH NEGATIVE STIFFNESS ABSORBERS

Vinícius Mauro de Souza Santos
Thiago de Paula Sales
Aeronautics Institute of Technology, Pç. Mal. Eduardo Gomes, 50 – Vila das Acácias, São José dos Campos, SP, Brazil
vinicius.santos@ga.ita.br, tpsales@ita.br

Morvan Ouisse
SUPMICROTECH, Université de Franche-Comté, CNRS, Institut FEMTO-ST, F-25000 Besançon, France
morvan.ouisse@femto-st.fr

Abstract. *Various researchers have demonstrated that Bragg-scattering can be suitably exploited to engineer periodic structures which show bandgaps, i.e., frequency ranges in which wave propagation is not allowed. This strategy is unsuitable for controlling wave propagation for some low-frequency applications, since large unit cells become required. Alternatively, locally resonant periodic structures can be designed to possess bandgaps in any frequency range. Nevertheless, these structures may not be adequate for some practical applications, due to the need for heavy resonators with low static stiffness, compromising desirable structural features, such as lightweight. Inertial amplification mechanisms (IAMs) have been employed as promising alternatives to the aforementioned techniques because they naturally exhibit forbidden zones in lower and broader frequency ranges. Hence, one studies the dynamic behavior of a periodic structure whose unit cell possesses IAM coupled to local resonators with negative stiffness absorbers. The aim is to investigate if Bragg-scattering and local resonance can be exploited to improve forbidden zones. The Wave-based Finite Element Method is used to compute free and forced responses. Predictions based on the Bloch-Floquet theorem were validated through the transmissibility response of a finite metastructure, which further confirmed the remarkable wave attenuation performance of the considered system and the bandgap merging.*

Keywords: *metamaterial, inertial amplification mechanism, negative stiffness absorber, periodic structures, wave-based finite element method*

1. INTRODUCTION

Acoustic and elastic metamaterials are specially engineered materials and devices which exhibit properties not naturally found in nature or conventional systems. As pointed out by Hussein *et al.* (2014), the prefix "meta", in this context, comes from the Greek language and indicates the notation of "after" or "beyond". Under these circumstances, metamaterials can be designed aiming to exploit the waveguiding appearance (Pal and Ruzzene, 2017), sub-middle-high-wavelength bandgap formation (Wang *et al.*, 2019; Mizukami *et al.*, 2021), confinement and mode localization phenomena (Sheng *et al.*, 2003; Wu *et al.*, 2009), invisibility cloaks (Ning *et al.*, 2020), and some negative equivalent properties such as refractive index, elastic modulus, and Poisson's ratio (Gao *et al.*, 2022).

Probably, in the field of vibration attenuation, the bandgaps are the most studied phenomena exhibited by metamaterials to prohibit wave propagation in some frequency ranges. Such forbidden zones can be realized by means of Bragg-scattering (Nobrega *et al.*, 2016), local resonance (Deng *et al.*, 2022) and inertial amplification mechanisms (IAMs) (Yuksel and Yilmaz, 2015). If one wants to couple a metamaterial with a conventional engineering system or even design a structure that behaves as a metamaterial on its own, referred to as a metastructure, each of the previously mentioned bandgap generation mechanisms can be utilized for specific engineering applications. For example, Bragg-scattering phenomenon can be useful to control wave propagation characteristics in higher frequency ranges, since not-so-large unit cells are required for this application (Krushynska *et al.*, 2017); spatially arranged local resonators are suitable to tune the bandgap width and location more easily (Wang *et al.*, 2019); and IAMs were recently exploited to control elastic waves propagation in lower frequency ranges without harm structural worthiness (Mizukami *et al.*, 2021). Of course some works have already investigated the dynamic behavior of a resulting system, by relying on coupled bandgaps generation mechanisms.

Jin *et al.* (2022), for example, proposed a layered honeycomb metastructure with an ultra-wide coupled bandgap ensuing from Bragg-scattering and local resonance. In a few words, the metamaterial presented by the authors was built from a local resonant phononic crystal, in which a heavy block was seated to a rubber one, coupled to a material fabricated by casting liquid two-phase silicone rubber. It was argued that bandgaps resulting from spatially arranged local resonators

are usually narrow when a factual engineering design is used, i.e., using a resonator with low mass. Thus, it is very challenging to achieve a wide forbidden zone based on local resonance in the low-frequency range, which is necessary for several engineering applications, such as those involved with noise, vibration, and harshness (NVH), because the bandgap width will be naturally small. This, for instance, harms the effectiveness of attenuation zones ensuing from local resonance for practical problems. In addition, Jin *et al.* (2022) pointed out that Bragg-bandgaps width and position can be controlled mainly by the length of the unit cell along the direction of wave propagation; however, they are usually located in higher frequency bands for not-so-large lattice constant, which may not be useful for some vibroacoustic applications. These limitations of Bragg-scattering and local resonance phenomena to generate bandgaps can be reasonably overcome by exploiting their individual potentialities (Jin *et al.*, 2022).

Also, in the context of metamaterials, negative stiffness absorbers (NSAs), also called negative stiffness devices (NSDs), have been extensively studied as novel mechanisms for controlling vibration levels in structural systems such as bridges and long cables (Zhou *et al.*, 2020). However, while much research has been dedicated to theoretical aspects, practical realizations of such devices are rare due to their hard conceptualization and implementation. Despite that, in a recent-related study, a NSD with adjustable negative stiffness based on a pre-compressed spring and a lever beam was proposed (Chen *et al.*, 2023). Authors experimentally tested the NSD to improve cable damping and demonstrated the feasibility of their theoretical findings. The NSD was investigated in parallel and series with commonly used damping elements, such as viscoelastic and high-damping rubber. Additionally, Chen *et al.* (2023) introduced several formulae that are useful for the optimal design of these mechanical vibration absorbers with negative stiffness.

Xiao *et al.* (2023) investigated locally resonant metamaterials (LRMs) with negative stiffness combined rotationally and transversely to a traditional beam-type host structure. Initially, a monatomic local resonator was utilized, along with a damping device, resulting in the resonator being referred by Xiao *et al.* (2023) to as NSA due to its energy absorption properties. The authors showed that rotational coupling-like applications between the host beam and the resonator can be used to move the stop band lower bound to smaller frequencies, just by increasing the resonator's damping properties. On the other hand, Xiao *et al.* (2023) argued that transversal coupling-like schemes can be employed to generate wider forbidden zones in higher frequency ranges than those generated with the rotational coupling strategy, by varying the same damping parameters used in the rotational coupling. Of course, these findings indicate that the rotational coupling scheme between a host beam and the NSA performs better in lower frequencies compared to the transversal configuration. Furthermore, various parametric studies were conducted regarding a host beam rotationally coupled to the NSAs, which clearly demonstrated the influences of negative stiffness, outrigger length, and damping ratio in the effectiveness of the metamaterial, concerning wave attenuation performance. The phenomenon of bandgap merging was also studied by Xiao *et al.* (2023), and it was shown that damped diatomic systems with NSAs can be used to enlarge the bandgap width, compared with the case without negative stiffness elements. This latter realization proves that NSAs can be used as a means of enhancing wave attenuation properties of a beam-type metastructure.

Wang *et al.* (2019) proposed and experimentally tested a metamaterial rod with resonators containing negative-stiffness mechanisms employing mutually repelling permanent magnet rings and compressed linear elastic coil springs. They discussed that despite the fact that local resonators can be, in theory, easily designed so bandgaps result in lower frequency ranges, a traditional resonator-like scheme fails to create an ultra-low forbidden-zone — this arises because very heavy or extremely soft resonators are required, as discussed before. In addition, it was seen in numerical simulations (Wang *et al.*, 2019) that the decrease of the resonator's negative stiffness moves the bandgap to lower frequencies, that are considerably lower in comparison to the resonant frequency of the metamaterial rod without NSD. An experimental transmittance curve revealed that the rod's bandgap is much wider than theoretical findings computed by the Harmonic Balance Method. The authors attribute part of this mismatching due to springs' variability and assembly errors, which leaded to different resonant frequencies for the resonators, so that these multiple bandgaps merged into an ultra-wide (or robust) bandgap. This realization was shown to be useful to broaden bandgaps in several works (Timorian *et al.*, 2019; Fabro *et al.*, 2021), resulting in what one knows as rainbow metamaterials.

In light of the aforementioned, this work aims to combine a specially designed unit cell possessing an IAM to a one degree of freedom (DoF) resonator portraying NSA. By leveraging the advantages of both IAM and local resonance, this research seeks to generate low-frequency bandgaps and widen these regions of attenuation for vibroacoustic applications. The IAM unit cell we adopted is very similar to the one designed by Mizukami *et al.* (2021), while the resonator scheme was inspired by the work of Xiao *et al.* (2023). The one DoF resonator is constructed by connecting a linear elastic spring to a mass, which in turn is connected to a damper. Additionally, a negative stiffness spring is connected in parallel to the damper. In such circumstances, one aims to study the dynamic behavior of the resulting metastructure, shown in Fig. 1, with respect to longitudinal waves. To the best of our knowledge, combining a unit cell owing IAM to a NSD has never been investigated before. Resonant devices utilizing NSAs were studied recently, as discussed previously, and various works indicated the possibility of easily tuning the position and width of forbidden zones generated in host structures through NSAs, highlighting their potential applications in structural dynamics. Following this reasoning, NSDs might be a relevant mechanism to tune the position and width of a bandgap ensuing from a metastructure with IAM, even after the design of the unit cell, which is usually performed by topological optimization. In addition, understanding the dynamic

behavior of a metamaterial-type structure, owning IAMs and NSAs, can be valuable to assess the viability of its use as an appendage to conventional systems, aiming to reduce and control wave propagation behavior in the latter, for example.

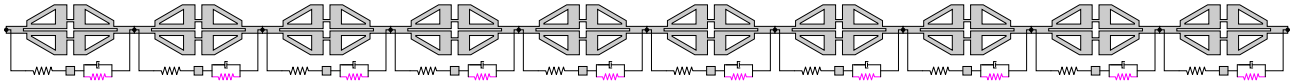

Figure 1: A metastructure assembled based on unit cells possessing IAMs combined longitudinally to a one DoF local resonator with negative stiffness (represented in magenta).

Beyond this introduction, this work has been divided into five sections. First, in Section 2 we briefly review the Wave-based Finite Element Method (WFEM), which was used in the modeling of the periodic metastructure possessing IAM and NSD shown in Fig. 1. Dispersion curves and longitudinal transmissibilities are presented in Section 3. Discussions about the dynamics of the coupled system are supplied, as well. A summary of our findings and conclusions is given in Section 4. Acknowledgments and references are provided at last.

2. MODELING

The one-dimensional periodic structure portrayed in Fig. 1, with $N = 10$ unit cells, can be modeled by means of the WFEM simply to reduce computational time during simulations, compared to conventional finite elements (FEs), for example. The resonator's properties are the positive and negative spring stiffnesses (k and k_{NS}), mass (m), and viscous damping coefficient (c). In such a case, one considers that a unit cell of the lattice is meshed by employing traditional FEs, as depicted in Fig. 2. The degrees of freedom (DoFs) and loads of this meshed unit cell are then partitioned with respect to their position in the cell, denoted as $\mathbf{q}_j$ and $\mathbf{F}_j$, respectively, for $j \in \{\mathrm{L}, \mathrm{R}, \mathrm{I}\}$. Here, L and R identify the sets of DoFs and loads which are located at the interfaces of the cell, specifically the left and right boundaries, while I refers to internal quantities. Figure 2 also depicts the longitudinal DoF of the resonator, u_m, translational DoFs related to a particular node s of the IAM, say, u_{s} and v_{s} — two DoFs per node —, and the nodes that couple the IAM with the NSA device, namely nodes 1 and n. For the sake of simplicity, one assumes that the total number of nodes of the IAM unit cell corresponds to n and related DoFs are organized ascendingly from 1 to $2n$.

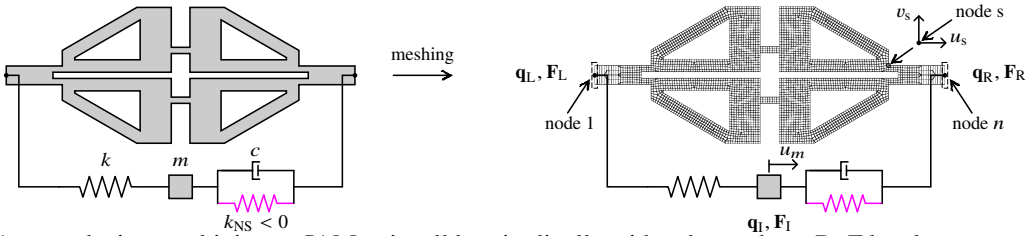

Figure 2: A meta-device combining an IAM unit cell longitudinally with a damped one DoF local resonator with negative stiffness (left) and their FE mesh (right). Negative spring stiffness is represented in magenta.

Accordingly, the equations of motion of the unit cell seen in Fig. 2 can be written as $(\mathbf{M}+\overline{\mathbf{M}})\ddot{\mathbf{q}}+(\mathbf{C}+\overline{\mathbf{C}})\dot{\mathbf{q}}+(\mathbf{K}+\overline{\mathbf{K}})\mathbf{q} = \mathbf{f}$, where $\ddot{\mathbf{q}}$, $\dot{\mathbf{q}}$, $\mathbf{q}$, and $\mathbf{f}$ are acceleration, velocity, displacement, and load vectors of size $2n+1 \times 1$; $\mathbf{M}$, $\mathbf{C}$ and $\mathbf{K}$ are matrices of mass, damping and stiffness which refer to the dynamics of the baseline IAM unit cell, of size $2n+1 \times 2n+1$, extracted from FE software and padded with one zero row, and one zero column; and $\overline{\mathbf{M}}$, $\overline{\mathbf{C}}$ and $\overline{\mathbf{K}}$ are written as:

$$\overline{\mathbf{M}} = \begin{array}{c} \begin{matrix} u_1 & v_1 & \cdots & u_n & v_n & u_m \end{matrix} \\ \begin{bmatrix} 0 & 0 & & 0 & 0 & 0 \\ 0 & 0 & & 0 & 0 & 0 \\ & & \ddots & & & \\ 0 & 0 & & 0 & 0 & 0 \\ 0 & 0 & & 0 & 0 & 0 \\ 0 & 0 & & 0 & 0 & m \end{bmatrix} \end{array} \begin{matrix} u_1 \\ v_1 \\ \vdots \\ u_n \\ v_n \\ u_m \end{matrix}, \quad \overline{\mathbf{C}} = \begin{array}{c} \begin{matrix} u_1 & v_1 & \cdots & u_n & v_n & u_m \end{matrix} \\ \begin{bmatrix} 0 & 0 & & 0 & 0 & 0 \\ 0 & 0 & & 0 & 0 & 0 \\ & & \ddots & & & \\ 0 & 0 & & c & 0 & -c \\ 0 & 0 & & 0 & 0 & 0 \\ 0 & 0 & & -c & 0 & c \end{bmatrix} \end{array} \begin{matrix} u_1 \\ v_1 \\ \vdots \\ u_n \\ v_n \\ u_m \end{matrix},$$

$$\overline{\mathbf{K}} = \begin{array}{c} \begin{matrix} u_1 & v_1 & \cdots & u_n & v_n & u_m \end{matrix} \\ \begin{bmatrix} k & 0 & & 0 & 0 & -k \\ 0 & 0 & & 0 & 0 & 0 \\ & & \ddots & & & 0 \\ 0 & 0 & & k_{\mathrm{NS}} & 0 & -k_{\mathrm{NS}} \\ 0 & 0 & & 0 & 0 & 0 \\ -k & 0 & & -k_{\mathrm{NS}} & 0 & k + k_{\mathrm{NS}} \end{bmatrix} \end{array} \begin{matrix} u_1 \\ v_1 \\ \vdots \\ u_n \\ v_n \\ u_m \end{matrix}. \quad (1)$$

In the frequency domain, one can write the unit cell's equations of motion as $\mathbf{Dq} = \mathbf{F}$, with $\mathbf{D} = -\omega^2(\mathbf{M}+\overline{\mathbf{M}}) + \mathrm{i}\omega(\mathbf{C}+\overline{\mathbf{C}}) + (\mathbf{K}+\overline{\mathbf{K}})$ being its dynamic stiffness matrix, i the imaginary unit, and ω the circular frequency (Fabro *et al.*, 2019). By considering the previously established partitions regarding the location of DoFs and loads in the considered unit cell, cf. Fig. 2, we are able to appropriately rewrite the dynamic stiffness matrix, as well as the corresponding displacement and load vectors. After condensing internal DoFs and performing various tedious mathematical manipulations, one arrives at the subsequent relation between adjacent unit cells, specifically (n) and $(n+1)$:

$$\mathbf{u}_{\mathrm{L}}^{(n+1)} = \mathbf{S}\mathbf{u}_{\mathrm{L}}^{(n)} + \mathbf{b}^{(n)}, \tag{2}$$

where $\mathbf{u}$ and $\mathbf{S}$ are known as the state vector and the unit cell transfer matrix, respectively, and $\mathbf{b}$ is a vector that collects externally applied loads (Hoang *et al.*, 2020). From the recurrence relation embedded in Eq. (2), one can derive the following relationships that will support the subsequent mathematical developments:

$$\mathbf{u}_{\mathrm{L}}^{(n+1)} = \mathbf{S}^n\mathbf{u}_{\mathrm{L}}^{(1)} + \sum_{k=1}^{n}\mathbf{S}^{n-k}\mathbf{b}^{(k)}, \qquad \mathbf{u}_{\mathrm{L}}^{(N+1)} = \mathbf{S}^{N+1-n}\mathbf{u}_{\mathrm{L}}^{(n)} + \sum_{k=n}^{N}\mathbf{S}^{N-k}\mathbf{b}^{(k)}. \tag{3}$$

Periodic boundary conditions (BCs) can be resorted using the Bloch-Floquet theorem, i.e., $\mathbf{u}_{\mathrm{L}}^{(n+1)} = \exp(-\mathrm{i}k_j\Delta)\mathbf{u}_{\mathrm{L}}^{(n)} = \mu_j\mathbf{u}_{\mathrm{L}}^{(n)}$, where Δ denotes the length of the unit cell along the direction of wave propagation, k_j represents the j-th wavenumber, and μ_j corresponds to its corresponding propagation constant (Goto *et al.*, 2020). By leveraging Eq. (2) and the Bloch-Floquet theorem, one obtains a standard eigenvalue problem, written as $(\mathbf{S}-\mu_j\mathbf{I})\boldsymbol{\phi}_j = \mathbf{0}$ — $\mathbf{I}$ represents the identity matrix —, whose solutions are the eigenpairs μ_j and $\boldsymbol{\phi}_j$ ($j = 1, ..., 2n_b$), being n_b the number of DoFs pertaining to the left (or right) interface of the unit cell (in our case $n_b = 6$, cf. Fig. 2). After the computation of propagation constants, wavenumbers can be obtained using $k_j = (\ln\mu_j)/(-\mathrm{i}\Delta)$. In the absence of any kind of damping, bandgaps can be identified for the frequency ranges in which $\mathrm{Im}\{k_j\} \neq 0$. Otherwise, the indicator of minimal evanescence ratio, defined as (Collet *et al.*, 2011):

$$\mathrm{Ind}\,(\omega) = \min_j \frac{|\mathrm{Im}\,\{k_j\}|}{|k_j|}, \tag{4}$$

may be used. In such a case, the attenuation zones are defined for the frequencies in which $\mathrm{Ind}\,(\omega)$ is greater than a threshold value $\mathrm{Ind_T}$ selected on a case-by-case basis. For the considered system, $\mathrm{Ind_T}$ is specified in Section 3.

In some cases, the standard eigenvalue problem encountered earlier is solved wrongly due to ill-conditioning issues. These arise because the state vector includes quantities associated with DoFs and loads, which may have significantly different magnitudes. As a result, an alternative well-conditioned formulation of the aforementioned standard eigenvalue problem can be written, exploiting the symplectic nature of matrix $\mathbf{S}$ (Zhong and Williams, 1995):

$$\left(\mathbf{A}-\lambda_j\mathbf{B}\right)\mathbf{z}_j = \mathbf{0}, \qquad \text{where} \qquad \mathbf{A} = \mathbf{NJL}^{\mathrm{T}} + \mathbf{LJN}^{\mathrm{T}}, \qquad \mathbf{B} = \mathbf{LJL}^{\mathrm{T}}; \tag{5}$$

and λ_j and $\mathbf{z}_j$ correspond to the eigenvalues and eigenvectors of the alternative, better-conditioned eigenproblem. Expressions for $\mathbf{N}$, $\mathbf{J}$, and $\mathbf{L}$ can be found elsewhere (Mencik and Duhamel, 2015).

Furthermore, since large condition numbers of $\mathbf{A}$ or $\mathbf{B}$ indicate a nearly singular problem, one can further alleviate numerical issues by employing the following methodology. If $\mathrm{cond}\,(\mathbf{A}) < \mathrm{cond}\,(\mathbf{B})$, where $\mathrm{cond}\,(.)$ denotes the condition number of a matrix, it is preferable to solve (Waki *et al.*, 2006):

$$\left(\mathbf{A}^{-1}\mathbf{B}-\hat{\lambda}_j\mathbf{I}\right)\mathbf{z}_j = 0, \tag{6}$$

whose solutions provide the inverse eigenvalues and corresponding eigenvectors, namely $\hat{\lambda}_j \equiv 1/\lambda_j$ and $\mathbf{z}_j$, respectively. Additionally, practice experience indicates that when $|\mathrm{Im}\{\hat{\lambda}_j\}| \to 0$ and $|\mathrm{Im}\{\hat{\lambda}_j\}| \neq 0$, $\hat{\lambda}_j \approx \mathrm{Re}\{\hat{\lambda}_j\}$.

It can also be shown that $\lambda_j = \mu_j + 1/\mu_j$, such that $\mu_j = [\lambda_j \pm (\lambda_j^2-4)^{0.5}]/2$ (Mencik and Ichchou, 2005). The eigenvectors of the original eigenvalue problem, $\boldsymbol{\phi}_j$, can be retrieved following the procedure outlined in (Mencik and Duhamel, 2015).

Eigensolutions computed before can be then grouped into matrices, according to the direction of wave propagation, i.e., into those related to positive-, $(\mu_j, \boldsymbol{\phi}_j)$, and negative-going waves, $(\mu_j^*, \boldsymbol{\phi}_j^*)$ ($j = 1, ..., n_b$) (Duhamel *et al.*, 2006; Waki *et al.*, 2009), so that one obtains:

$$\boldsymbol{\mu} = \mathrm{diag}(\mu_1, \ldots, \mu_{n_b}), \quad \boldsymbol{\mu}^* = \mathrm{diag}(\mu_1^*, \ldots, \mu_{n_b}^*), \quad \boldsymbol{\Phi} = [\boldsymbol{\phi}_1 \ldots \boldsymbol{\phi}_{n_b}] = \begin{bmatrix}\boldsymbol{\Phi}_q \\ \boldsymbol{\Phi}_F\end{bmatrix}, \quad \boldsymbol{\Phi}^* = [\boldsymbol{\phi}_1^* \ldots \boldsymbol{\phi}_{n_b}^*] = \begin{bmatrix}\boldsymbol{\Phi}_q^* \\ \boldsymbol{\Phi}_F^*\end{bmatrix}, \tag{7}$$

with q and F used to identify partitions of $\boldsymbol{\Phi}$ and $\boldsymbol{\Phi}^*$ related to DoFs and loads. At this point, one highlights that any frequency-tracking procedure, such as the modal assurance criterion (MAC) or another one that exploits the symplectic

nature of $\mathbf{S}$ can be employed to track the wavemodes with respect to frequency (Mencik, 2010). In addition, it is important to note that the eigenvectors must be properly normalized (Mencik, 2014) so expressions presented afterward are valid.

The forced response of the periodic structure can be computed by expressing the state vector and the vector of externally applied loads as a linear combination of wave amplitudes, utilizing the computed wave modes. Building upon this expansion, one can write:

$$\mathbf{u}_{\mathrm{L}}^{(n)} = \boldsymbol{\Phi}\mathbf{Q}^{(n)} + \boldsymbol{\Phi}^{*}\mathbf{Q}^{*(n)}, \tag{8}$$

and

$$\mathbf{b}^{(n)} = \boldsymbol{\Phi}\mathbf{Q}_{B}^{(n)} + \boldsymbol{\Phi}^{*}\mathbf{Q}_{B}^{*(n)}, \tag{9}$$

where $\mathbf{Q}^{(n)}$, $\mathbf{Q}^{*(n)}$, $\mathbf{Q}_{B}^{(n)}$ and $\mathbf{Q}_{B}^{*(n)}$ are amplitude vectors. By manipulating Eq. (3) one arrives at:

$$\mathbf{Q}^{(n)} = \boldsymbol{\mu}^{n-1}\mathbf{Q}^{(1)} + \sum_{k=1}^{n-1} \boldsymbol{\mu}^{n-k-1}\mathbf{Q}_{B}^{(k)}, \tag{10}$$

$$\mathbf{Q}^{*(n)} = \boldsymbol{\mu}^{N+1-n}\mathbf{Q}^{*(N+1)} - \sum_{k=n}^{N} \boldsymbol{\mu}^{k-n+1}\mathbf{Q}_{B}^{*(k)}, \tag{11}$$

being $\mathbf{Q}_{B}^{(k)}$ and $\mathbf{Q}_{B}^{*(k)}$ obtained after manipulating Eq. (9), given by:

$$\mathbf{Q}_{B}^{(k)} = \left(\boldsymbol{\mu}\boldsymbol{\Phi}_{q}^{*\mathrm{T}}\mathbf{D}_{\mathrm{LI}} + \boldsymbol{\Phi}_{q}^{*\mathrm{T}}\mathbf{D}_{\mathrm{RI}}\right)\mathbf{F}_{\mathrm{I}}^{(k)} - \boldsymbol{\Phi}_{q}^{*\mathrm{T}}\mathbf{F}_{B}^{(k)}, \tag{12}$$

$$\mathbf{Q}_{B}^{*(k)} = -\left(\boldsymbol{\mu}^{*}\boldsymbol{\Phi}_{q}^{\mathrm{T}}\mathbf{D}_{\mathrm{LI}} + \boldsymbol{\Phi}_{q}^{\mathrm{T}}\mathbf{D}_{\mathrm{RI}}\right)\mathbf{F}_{\mathrm{I}}^{(k)} + \boldsymbol{\Phi}_{q}^{\mathrm{T}}\mathbf{F}_{B}^{(k)}. \tag{13}$$

Once the state vector $\mathbf{u}_{\mathrm{L}}^{(n)}$ is written in terms of DoFs and loads, say $\mathbf{q}_{\mathrm{L}}^{(n)}$ and $\mathbf{F}_{\mathrm{L}}^{(n)}$, and considering the partitions introduced in Eq. (7), combining Eqs. (8), (10), and (11) yields the following result:

$$\mathbf{q}_{\mathrm{L}}^{(n)} = \boldsymbol{\Phi}_{q}\boldsymbol{\mu}^{n-1}\mathbf{Q} + \boldsymbol{\Phi}_{q}^{*}\boldsymbol{\mu}^{N+1-n}\mathbf{Q}^{*} + \boldsymbol{\Phi}_{q}\sum_{k=1}^{n-1}\boldsymbol{\mu}^{n-k-1}\mathbf{Q}_{B}^{(k)} - \boldsymbol{\Phi}_{q}^{*}\sum_{k=n}^{N}\boldsymbol{\mu}^{k+1-n}\mathbf{Q}_{B}^{*(k)}, \tag{14}$$

$$-\mathbf{F}_{\mathrm{L}}^{(n)} = \boldsymbol{\Phi}_{F}\boldsymbol{\mu}^{n-1}\mathbf{Q} + \boldsymbol{\Phi}_{F}^{*}\boldsymbol{\mu}^{N+1-n}\mathbf{Q}^{*} + \boldsymbol{\Phi}_{F}\sum_{k=1}^{n-1}\boldsymbol{\mu}^{n-k-1}\mathbf{Q}_{B}^{(k)} - \boldsymbol{\Phi}_{F}^{*}\sum_{k=n}^{N}\boldsymbol{\mu}^{k+1-n}\mathbf{Q}_{B}^{*(k)}, \tag{15}$$

with $\mathbf{Q} \equiv \mathbf{Q}^{(1)}$ and $\mathbf{Q}^{*} \equiv \mathbf{Q}^{*(N+1)}$. Equations (14) and (15) can be utilized alongside BCs to establish a linear system for $\mathbf{Q}$ and $\mathbf{Q}^{*}$. Solving this system enables the determination of any response of the periodic structure under consideration.

3. NUMERICAL SIMULATIONS

Numerical experiments portrayed in this section consider the FE mesh depicted in Fig. 2, whose dimensions are shown in Fig. 3, to model the metastructure seen in Fig. 1. As can be noticed from Fig. 2, triangular and quadrilateral elements with 2 translational DoFs per node were used to mesh the geometry. The baseline unit cell FE matrices, $\mathbf{M}$ and $\mathbf{K}$, were extracted from FE software assuming plane stress state, with a thickness of 30 mm. Damping is not taken into account for the baseline unit cell ($\mathbf{C} = \mathbf{0}$) to study the isolated effect of the NSA in the dynamic behavior of the meta-device shown in Fig. 2, regarding vibration attenuation properties. In addition, the baseline unit cell is regarded as being fabricated using additive manufacturing techniques, specifically using polylactic acid (PLA), for which its elastic modulus, specific mass and Poisson's ratio are 2.35 GPa, 1037.5 kg m^{-3}, and 0.3, respectively. Furthermore, a reduced wave basis of six left- and right-going wave modes, i.e., $n_b = 3$, was employed to characterize the dynamic behavior of the cell incorporating IAM. This choice was made because highly evanescent wave modes often introduce numerical challenges in calculations and have negligible contributions to the response of the meta-device under investigation, which functions as a waveguide.

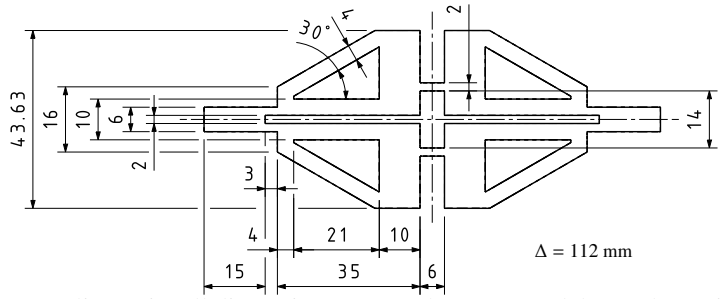

Figure 3: Baseline unit cell dimensions (mm) whose FE model was shown in Fig. 2.

First, employing the theory reviewed in Section 2, one is able to compute the dispersion curves for the undamped baseline unit cell portrayed in Fig. 3. Since the analyzed system does not exhibit any non-reciprocal behavior in terms of

wave propagation characteristics, the dispersion curves are symmetric with respect to the abscissa axis. For this reason, Fig. 4 illustrates the plot of positive values of $\mathrm{Re}\{k_j\}$ with negative values of $\mathrm{Im}\{k_j\}$. These curves are related to longitudinal and bending wave modes that propagate or decay in space in the left and right directions. Of particular interest in this work, is the pair of wave modes that is related to longitudinal motion, to exploit the coupling scheme portrayed in Fig. 1 between the baseline IAM unit cell and the NSA. It should be noted that in this specific coupling configuration, the resonator solely affects the longitudinal motion of the meta-device illustrated in Fig. 2. Accordingly, results shown next correspond to the longitudinal wave mode, for which there exist an attenuation zone between 242 and 685 Hz ($\mathrm{Im}\{k_j\} \neq 0$) in Fig. 4, highlighted by the gray shaded area.

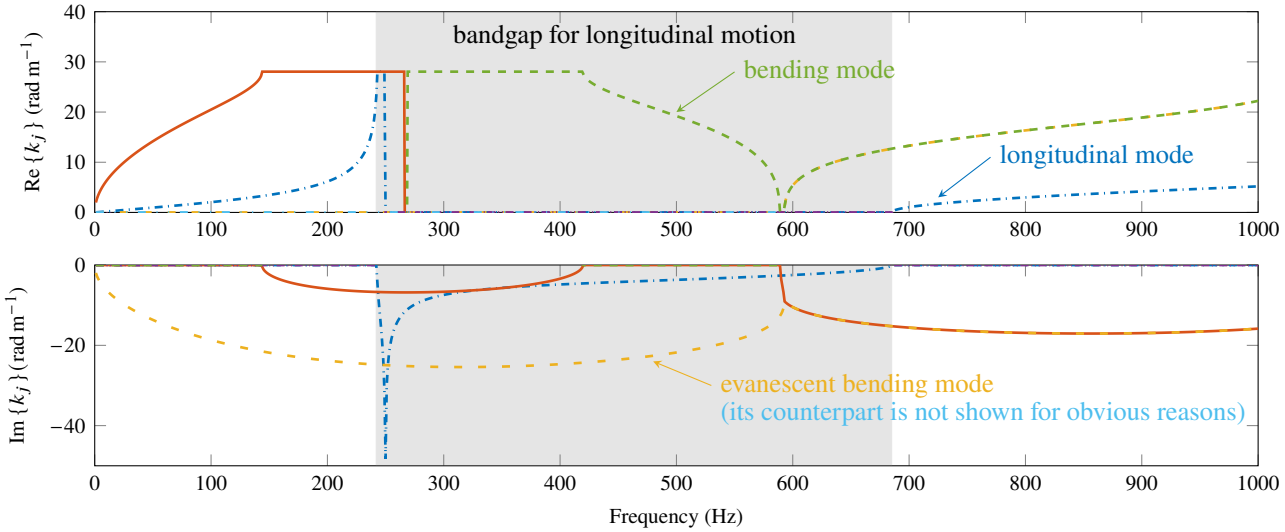

Figure 4: Dispersion curves (positive values of $\mathrm{Re}\{k_j\}$ and negative values of $\mathrm{Im}\{k_j\}$) computed for the undamped ($\mathbf{C} = \mathbf{0}$) baseline unit cell incorporating IAM depicted in Fig. 3 through the Bloch-Floquet theorem. The correspondence between the wavenumbers depicted in $\mathrm{Re}\{k_j\}$ and $\mathrm{Im}\{k_j\}$ is illustrated by the dispersion curves with matching colors.

In this study, it is initially assumed that the viscous damping coefficient and negative stiffness are zero, $c = k_{\mathrm{NS}} = 0$, for the meta-device depicted in Fig. 2. Furthermore, the mass of the resonator m is related to the unit cell mass, denoted as $m_{\mathrm{IAM}} = 60\,\mathrm{g}$, through the parameter $\gamma = m/m_{\mathrm{IAM}}$. Thus, let the resonator's natural frequency, $\omega = \sqrt{k/m} = \sqrt{k/(\gamma\, m_{\mathrm{IAM}})}$, be tuned at 220 Hz, for $\gamma \in \{0.2, 0.4, 0.6, 0.8, 1, 5\}$, so that the positive spring stiffness is obtained from $k = \gamma\omega^2 m_{\mathrm{IAM}}$. In this case, Fig. 5 displays the corresponding imaginary part of left-going longitudinal wave modes and the evolution of the bandgap width. As can be noticed from Fig. 5, an attenuation zone opens near the resonator's natural frequency in all considered cases. In addition, as one may expect, the increase of the resonator's mass corroborates to widen the attenuation

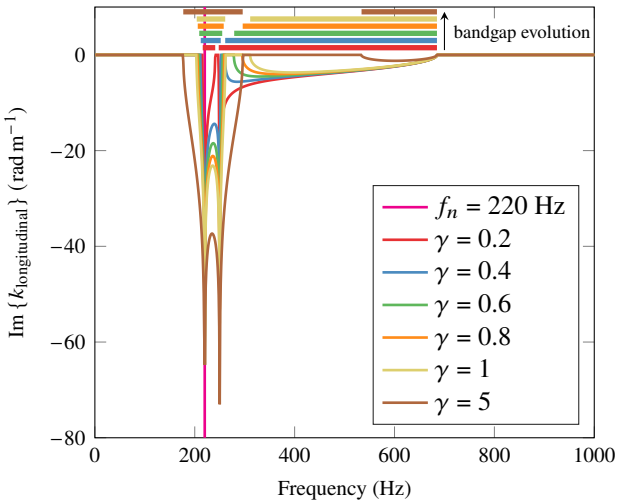

Figure 5: Imaginary part of left-going longitudinal wave modes and the evolution of the bandgap width computed for the undamped ($\mathbf{C} = \mathbf{0}$) unit cell incorporating IAM depicted in Fig. 2 through the Bloch-Floquet theorem. The resonator's viscous damping coefficient and negative stiffness were taken as zero ($c = k_{\mathrm{NS}} = 0$). Correspondence between the wavenumbers, bandgap evolution, and the associated legends is established through color matching.

zone ensuing of local resonance. However, the same figure shows that at a certain condition, an excessive increase of $m \propto \gamma$ greatly reduces the Bragg-bandgap width resulting from the undamped baseline unit cell which possesses IAM. Lastly, it should be mentioned that the upper bounds of the bandgaps associated with the IAM remain unaffected for all cases depicted in Fig. 5. Since in most engineering applications lightweight design is of concern, γ was selected as 0.2 for the numerical experiments shown afterwards. This value also provides a good compromise between a wider bandgap caused by the IAM and the formation of the tuned attenuation zone at approximately 220 Hz.

The inclusion of the viscous damping coefficient is now taken into account in our simulations while keeping $k_{\mathrm{NS}} = 0$. This allows us to investigate the dissipation properties of the unit cell portrayed in Fig. 2, which arise from the resonator's dynamics. As discussed earlier in Section 2, the indicator of minimal evanescence ratio was utilized to define the attenuation zones in the presence of damping, given that all wave numbers are complex in such scenario. The threshold value $\mathrm{Ind}_{\mathrm{T}}$ was selected based on the following expression (Salsa *et al.*, 2023):

$$\mathrm{Ind}_{\mathrm{T}} = 5\% \cdot (\max_{\omega} \mathrm{Ind}(\omega) - \min_{\omega} \mathrm{Ind}(\omega)). \tag{16}$$

Thus, Fig. 6 depicts the dispersion curves corresponding to longitudinal wave modes for $c \in \{0.01, 0.1, 2, 4, 6, 8\}\,\mathrm{N\,s\,m^{-1}}$. As can be seen in Fig. 6, the inclusion of a viscous dashpot in series with the resonator, with c greater or equal than $2\,\mathrm{N\,s\,m^{-1}}$, proves to be an effective approach to merge the wider bandgap resulting from the IAM unit cell with the narrower one associated with local resonance. This results in the formation of a much broader coupled attenuation zone. In the context of wave manipulation in metamaterials, this strategy to merge two close bandgaps is what one knows as metadamping. Similar to what was seen earlier in Fig. 5, the upper bound of the forbidden zones ensuing from IAM remains unchanged for $c = 0.01$ and $c = 0.1\,\mathrm{N\,s\,m^{-1}}$ in Fig. 6. The same behavior persists when both bandgaps are merged into a wider one, that is, for values of the viscous damping coefficient equal to 2, 4, 6, and $8\,\mathrm{N\,s\,m^{-1}}$.

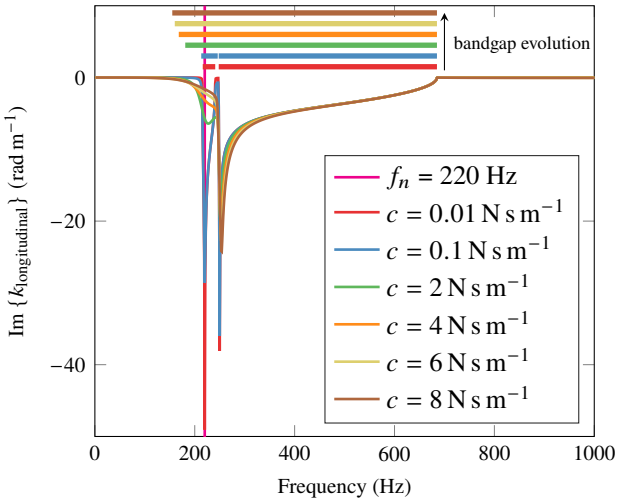

Figure 6: Imaginary part of left-going longitudinal wave modes and the evolution of the bandgap width computed for the unit cell incorporating IAM depicted in Fig. 2 through the Bloch-Floquet theorem. The resonator's negative stiffness was taken as zero ($k_{\mathrm{NS}} = 0$) and $\mathbf{C} = \mathbf{0}$. Correspondence between the wavenumbers, bandgap evolution, and the associated legends is established through color matching.

In order to provide a clearer understanding of the utilization of the indicator of minimal evanescence ratio for identifying the attenuation zones provided in Fig. 6, Fig. 7 shows the values of $\mathrm{Ind}\,(\omega)$ and $\mathrm{Ind}_{\mathrm{T}}$ plotted against ω. As explained in Section 2, the attenuation zones exist at frequencies for which $\mathrm{Ind}\,(\omega) > \mathrm{Ind}_{\mathrm{T}}$. Therefore, results exhibited in Fig. 7, with support of those shown in Fig. 6, confirm the effectiveness of the methodology employed for identifying the attenuation zones in damped systems. Next, based on results presented in Figs. 6 and 7, to conduct further analyses, one fixes the viscous damping coefficient as $c = 2\,\mathrm{N\,s\,m^{-1}}$. From the considered cases, this value represents the minimum damping required to combine the bandgaps resulting from the IAM and local resonance.

Finally, parametric analyses are conducted to examine the impact of negative spring stiffness values on the dynamic behavior of the meta-device depicted in Fig. 2. For simplicity, let us assume that the negative stiffness spring value k_{NS} is related to the resonator's positive stiffness through the coefficient α, i.e., $k_{\mathrm{NS}} = -\alpha\, k$. Accordingly, Fig. 8 depicts the dispersion curves for left-going longitudinal wave-modes corresponding to $\alpha \in \{0.1, 0.2, 0.3, 0.4, 0.5, 1\}$. As one may notice from Fig. 8, small (absolute) values of negative stiffness, such as the one that arises when $\alpha = 0.1$, shift the coupled bandgap lower bound to smaller frequency ranges while leaving its upper bound unchanged. This behavior persists for $\alpha = 0.2$ and $\alpha = 0.3$. This occurs because the negative spring stiffness, when combined in parallel with a dashpot, as shown in the case depicted in Fig. 2, facilitates the dissipation of energy in the damper (Xiao *et al.*, 2023). However, raising

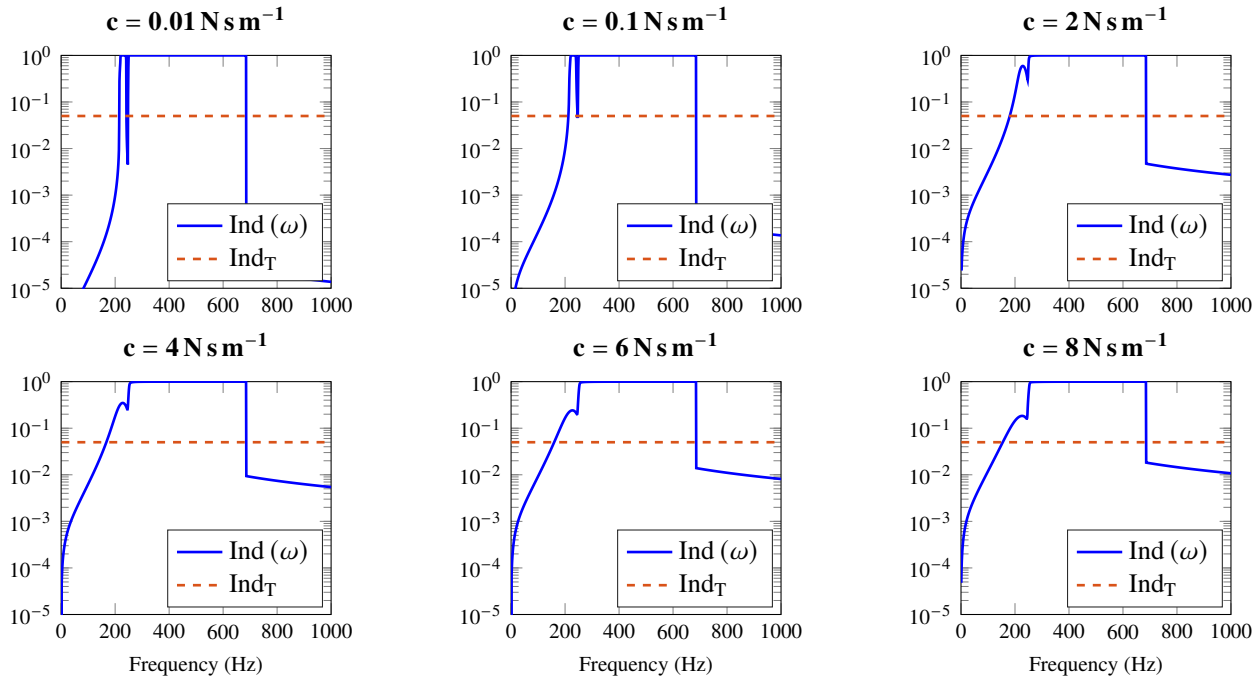

Figure 7: Indicators of minimal evanescence ratio and threshold values used to establish the attenuation zones seen in Fig. 6 for $c \in \{0.01, 0.1, 2, 4, 6, 8\}\,\mathrm{N\,s\,m^{-1}}$. Such forbidden zones are defined at frequencies for which $\mathrm{Ind}\,(\omega) > \mathrm{Ind_T}$.

the absolute value of the negative spring stiffness too much eventually splits the merged bandgaps, as can be seen for $\alpha = 0.4$, $\alpha = 0.5$, and $\alpha = 1$, while keeping the lower and upper bounds of the bandgap associated with the IAM unaltered. Moreover, making the negative spring stiffness value exactly equal to minus the positive spring stiffness, i.e., when $\alpha = 1$, causes the lower bound of the bandgap related to local resonance to shift towards approximately zero frequency. This realization comes at the cost of reducing the level of attenuation of the wave mode within the forbidden zone, as clearly observed in Fig. 8. It should be mentioned that the condition where $\alpha = 1$ results in a configuration of zero static stiffness for the NSA, which greatly impairs the practical use and implementation of the meta-device as a vibration absorber.

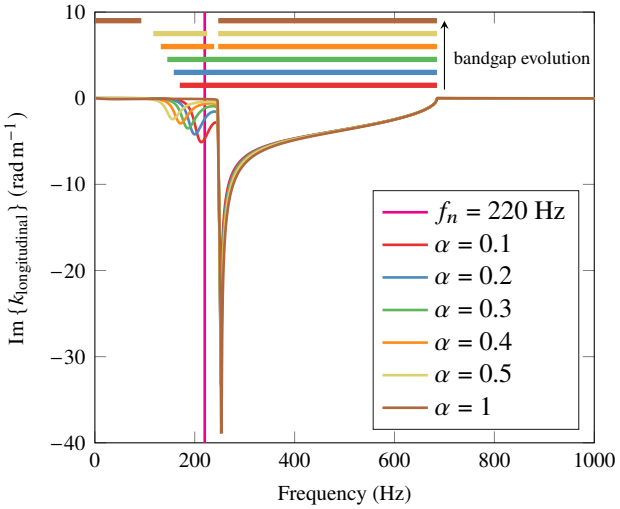

Figure 8: Imaginary part of left-going longitudinal wave modes and the evolution of the bandgap width computed for the unit cell incorporating IAM depicted in Fig. 2 through the Bloch-Floquet theorem ($\mathbf{C} = \mathbf{0}$). Correspondence between the wavenumbers, bandgap evolution, and the associated legends is established through color matching.

At last, one checks if the previously observed results are valid for a finite system with $N = 10$ unit cells, as represented in Fig. 1, by employing the theory discussed in Section 2 to compute a forced response. As a result, Fig. 9 illustrates, on the right, a transmissibility curve for the input and output locations schematically shown on the left. Here, we assumed $\gamma = 0.2$, $c = 2\,\mathrm{N\,s\,m^{-1}}$, and $\alpha = 0.2$. As predicted by the dispersion curve in Fig. 8 (for $\alpha = 0.2$), Fig. 9 shows on the right that the attenuation zone resulting from the IAM got merged with the forbidden zone associated with the NSA, which

arises from local resonance. This is true because the system's bandgap computed using the Bloch-Floquet theory and the indicator of minimal evanescence ratio, highlighted by the gray shaded area in Fig. 9, closely match the frequency range of attenuation in the transmissibility curve, where it is less than one.

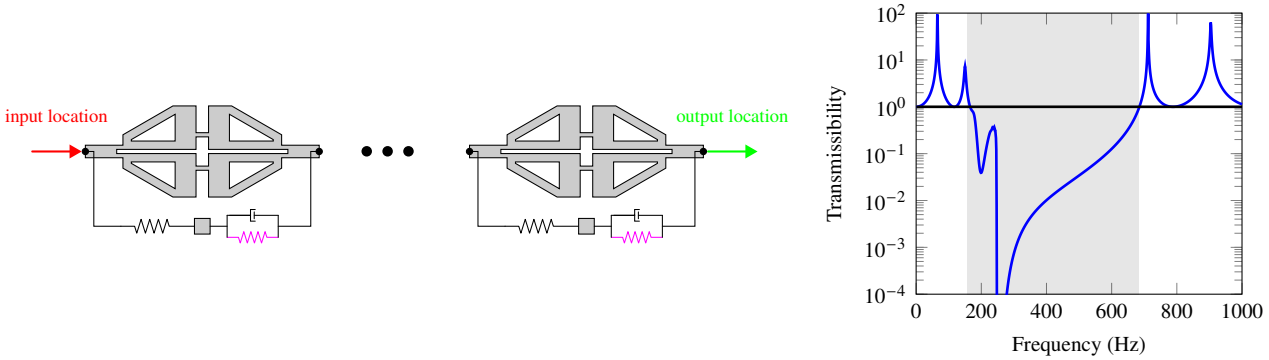

Figure 9: Input and output locations (on the left) used to calculate the forced response of the system portrayed in Fig. 1, which is shown on the right. Negative spring stiffness is represented in magenta.

4. CONCLUDING REMARKS

This article focuses on the longitudinal dynamic behavior of a unit cell that incorporates IAM coupled with a NSA. The baseline unit cell was designed through topological optimization and exhibits a wide bandgap for longitudinal wave modes in the low-frequency range, specifically between 242 and 685 Hz. Our study demonstrates that this attenuation range can be further enhanced by incorporating NSAs, even after the baseline unit cell design is optimized using algorithms. Numerical results reveal the potential to increase the bandgap width in a system that combines IAM and local resonance. It was observed that, in the investigated resonator-like scheme, the inclusion of a negative stiffness spring in parallel with a dashpot enhances the wave attenuation properties of the meta-device. This is due to the negative stiffness spring facilitating the motion between its terminals, thereby promoting energy dissipation in the dashpot. These findings present a promising approach for designing unit cells that incorporate IAMs and take advantage of NSAs, offering valuable opportunities for vibration mitigation in vibroacoustic problems.

5. ACKNOWLEDGEMENTS

V. M. S. Santos acknowledges his doctorate scholarship by the Brazilian Coordination for the Improvement of Higher Education Personnel (CAPES). V. M. S. Santos and T. P. Sales are grateful to the São Paulo Research Foundation (FAPESP) for its support to the thematic grant #18/15894-0, related to the "Periodic structure design and optimization for enhanced vibroacoustic performance: ENVIBRO" research project. M. Ouisse acknowledges the graduate school EIPHI (project ANR-17-EURE-0002).

6. REFERENCES

Chen, L., Liu, Z., Zou, Y., Wang, M., Nagarajaiah, S., Sun, F. and Sun, L., 2023. "Practical negative stiffness device with viscoelastic damper in parallel or series configuration for cable damping improvement". *J. Sound Vib.*, p. 117757. doi:10.1016/j.jsv.2023.117757.

Collet, M., Ouisse, M., Ruzzene, M. and Ichchou, M.N., 2011. "Floquet–Bloch decomposition for the computation of dispersion of two-dimensional periodic, damped mechanical systems". *Int. J. Solids Struct.*, Vol. 48, No. 20, pp. 2837–2848. doi:10.1016/j.ijsolstr.2011.06.002.

Deng, J., Guasch, O., Maxit, L. and Gao, N., 2022. "A metamaterial consisting of an acoustic black hole plate with local resonators for broadband vibration reduction". *J. Sound Vib.*, Vol. 526, p. 116803. doi:10.1016/j.jsv.2022.116803.

Duhamel, D., Mace, B.R. and Brennan, M.J., 2006. "Finite element analysis of the vibrations of waveguides and periodic structures". *J. Sound Vib.*, Vol. 294, No. 1-2, pp. 205–220. doi:10.1016/j.jsv.2005.11.014.

Fabro, A.T., Ferguson, N.S. and Mace, B.R., 2019. "Wave propagation in slowly varying waveguides using a finite element approach". *J. Sound Vib.*, Vol. 442, pp. 308–329. doi:10.1016/j.jsv.2018.11.004.

Fabro, A.T., Meng, H. and Chronopoulos, D., 2021. "Correlated disorder in rainbow metamaterials for vibration attenuation". *P. I. Mech. Eng. C-j. Mec.*, Vol. 235, No. 14, pp. 2610–2621. doi:10.1177/0954406220986596.

Gao, N., Zhang, Z., Deng, J., Guo, X., Cheng, B. and Hou, H., 2022. "Acoustic Metamaterials for Noise Reduction: A Review". *Adv. Mater. Technol.*, Vol. 7, No. 6, p. 2100698. doi:10.1002/admt.202100698.

Goto, A.M., Nóbrega, E.D., Pereira, F.N. and Santos, J.M.C.D., 2020. "Numerical and experimental investigation of

phononic crystals via wave-based higher-order rod models". *Int. J. Mech. Sci.*, Vol. 181, p. 105776. doi:10.1016/j.ijmecsci.2020.105776.

Hoang, T., Duhamel, D. and Foret, G., 2020. "Wave finite element method for waveguides and periodic structures subjected to arbitrary loads". *Finite Elem. Anal. Des.*, Vol. 179, p. 103437. doi:10.1016/j.finel.2020.103437.

Hussein, M.I., Leamy, M.J. and Ruzzene, M., 2014. "Dynamics of Phononic Materials and Structures: Historical Origins, Recent Progress, and Future Outlook". *Appl. Mech. Rev.*, Vol. 66, No. 4. doi:10.1115/1.4026911.

Jin, Y., Jia, X.Y., Wu, Q.Q., He, X., Yu, G.C., Wu, L.Z. and Luo, B., 2022. "Design of vibration isolators by using the Bragg scattering and local resonance band gaps in a layered honeycomb meta-structure". *J. Sound Vib.*, Vol. 521, p. 116721. doi:10.1016/j.jsv.2021.116721.

Krushynska, A.O., Miniaci, M., Bosia, F. and Pugno, N.M., 2017. "Coupling local resonance with Bragg band gaps in single-phase mechanical metamaterials". *Extreme Mech. Lett.*, Vol. 12, pp. 30–36. doi:10.1016/j.eml.2016.10.004.

Mencik, J.M., 2010. "On the low- and mid-frequency forced response of elastic structures using wave finite elements with one-dimensional propagation". *Comput. Struct.*, Vol. 88, No. 11-12, pp. 674–689. doi:10.1016/j.compstruc.2010.02.006.

Mencik, J.M., 2014. "New advances in the forced response computation of periodic structures using the wave finite element (WFE) method". *Comput. Mech.*, Vol. 54, No. 3, pp. 789–801. doi:10.1007/s00466-014-1033-1.

Mencik, J.M. and Duhamel, D., 2015. "A wave-based model reduction technique for the description of the dynamic behavior of periodic structures involving arbitrary-shaped substructures and large-sized finite element models". *Finite Elem. Anal. Des.*, Vol. 101, pp. 1–14. doi:10.1016/j.finel.2015.03.003.

Mencik, J.M. and Ichchou, M.N., 2005. "Multi-mode propagation and diffusion in structures through finite elements". *Eur. J. Mech. A. Solids*, Vol. 24, No. 5, pp. 877–898. doi:10.1016/j.euromechsol.2005.05.004.

Mizukami, K., Funaba, K. and Ogi, K., 2021. "Design and three-dimensional printing of carbon-fiber-composite elastic metamaterials with inertial amplification mechanisms". *J. Sound Vib.*, Vol. 513, p. 116412. doi:10.1016/j.jsv.2021.116412.

Ning, L., Wang, Y.Z. and Wang, Y.S., 2020. "Active control cloak of the elastic wave metamaterial". *Int. J. Solids Struct.*, Vol. 202, pp. 126–135. doi:10.1016/j.ijsolstr.2020.06.009.

Nobrega, E.D., Gautier, F., Pelat, A. and Santos, J.M.C.D., 2016. "Vibration band gaps for elastic metamaterial rods using wave finite element method". *Mech. Syst. Signal Pr.*, Vol. 79, pp. 192–202. doi:10.1016/j.ymssp.2016.02.059.

Pal, R.K. and Ruzzene, M., 2017. "Edge waves in plates with resonators: an elastic analogue of the quantum valley Hall effect". *New J. Phys.*, Vol. 19, No. 2, p. 025001. doi:10.1088/1367-2630/aa56a2.

Salsa, R., Sales, T.P. and Rade, D.A., 2023. "Optimization of Vibration Band Gaps in Damped Lattice Metamaterials". *Lat. Am. J. Solids Stru.*, Vol. 20. doi:doi.org/10.1590/1679-78257486.

Sheng, P., Zhang, X.X., Liu, Z. and Chan, C.T., 2003. "Locally resonant sonic materials". *Phys. B Condens. Matter*, Vol. 338, No. 1-4, pp. 201–205. doi:10.1016/s0921-4526(03)00487-3.

Timorian, S., Petrone, G., Rosa, S., Franco, F., Ouisse, M. and Bouhaddi, N., 2019. "Spectral analysis and structural response of periodic and quasi-periodic beams". *P. I. Mech. Eng. C-j. Mec.*, Vol. 233, No. 23-24, pp. 7498–7512. doi:10.1177/0954406219888948.

Waki, Y., Mace, B.R. and Brennan, M.J., 2006. "On Numerical Issues for the Wave/Finite Element Method". Technical Memorandum No. 964, University of Southampton, Institute of Sound & Vibration Research.

Waki, Y., Mace, B.R. and Brennan, M.J., 2009. "Free and forced vibrations of a tyre using a wave/finite element approach". *J. Sound Vib.*, Vol. 323, No. 3-5, pp. 737–756. doi:10.1016/j.jsv.2009.01.006.

Wang, K., Zhou, J., Wang, Q., Ouyang, H. and Xu, D., 2019. "Low-frequency band gaps in a metamaterial rod by negative-stiffness mechanisms: Design and experimental validation". *Appl. Phys. Lett.*, Vol. 114, No. 25, p. 251902. doi:10.1063/1.5099425.

Wu, T.C., Wu, T.T. and Hsu, J.C., 2009. "Waveguiding and frequency selection of Lamb waves in a plate with a periodic stubbed surface". *Phys. Rev. B*, Vol. 79, No. 10. doi:10.1103/physrevb.79.104306.

Xiao, L., Bursi, O.S., Wang, M., Nagarajaiah, S., Sun, F. and Du, X.L., 2023. "Metamaterial beams with negative stiffness absorbers and rotation: band-gap behavior and band-gap merging". *Eng. Struct.*, Vol. 280, p. 115702. doi:10.1016/j.engstruct.2023.115702.

Yuksel, O. and Yilmaz, C., 2015. "Shape optimization of phononic band gap structures incorporating inertial amplification mechanisms". *J. Sound Vib.*, Vol. 355, pp. 232–245. doi:10.1016/j.jsv.2015.06.016.

Zhong, W.X. and Williams, F.W., 1995. "On the direct solution of wave propagation for repetitive structures". *J. Sound Vib.*, Vol. 181, No. 3, pp. 485–501. doi:10.1006/jsvi.1995.0153.

Zhou, P., Liu, M. and Li, H., 2020. "A passive negative stiffness damper in series with a flexible support: Theoretical and experimental study". *Struct. Control Hlth.*, Vol. 27, No. 9. doi:10.1002/stc.2594.

7. RESPONSIBILITY NOTICE

The authors are solely responsible for the printed material included in this paper.